AIAA Guidance, Navigation, and Control Conference and Exhibit
15 - 18 August 2005, San Francisco, California

AIAA 2005-6244

Disturbance Filtering and Identification on the Naval Postgraduate School 3-Axis Spacecraft Simulator

Jimmy Lau[*], Sanjay S. Joshi[†],
University of California, Davis, California 95616

and

Brij N. Agrawal[‡], Jong-Woo Kim[§]
Naval Postgraduate School, Monterey, California 93943

This paper investigates spacecraft disturbance rejection filtering for both persistent and decaying disturbances. The current study both validates the previously developed "dipole" disturbance rejection filter on a realistic non-linear spacecraft model, and extends the results to a new class of decaying disturbances. Although not designed specifically for decaying disturbances, prior investigations have demonstrated that the traditional "dipole" disturbance rejection filter attenuates both persistent periodic disturbances and decaying disturbances. Here we introduce a new filter which we call the decaying disturbance rejection filter, which has greater attenuation than the traditional filter for decaying disturbances. The new filter is also based on the internal model principle like the traditional filter. Also, it is shown that both the traditional and the new filter are not robust to frequency uncertainty. As a result, new closed-loop system identification methods are introduced to experimentally identify the disturbance frequency to be used within the filter design for both filter types.

I. Introduction

A common challenge in spacecraft control is the mitigation of disturbances emanating from flexible appendages. In the present paper, disturbance rejection filtering is studied using the NPS Three Axis Simulator (TAS) testbed. The TAS was developed at the Naval Postgraduate School in Monterey, CA and is shown in Fig. 1. The purpose of the TAS was to prove a satellite's ability to redirect a laser originating from Earth, an aircraft, or another satellite to another location on Earth for communication or defense applications. A satellite utilizing lasers requires exceptional acquisition, pointing and tracking capabilities. On-going research has been conducted to study fine acquisition, pointing, and tracking requirements[1, 2]. Recently, a flexible appendage has been added to the TAS to serve as a source of vibration disturbance to the spacecraft bus for vibration disturbance studies.

[*] Graduate Research Assistant, Department of Mechanical and Aeronautical Engineering, University of California, Davis
[†] Corresponding Author, Professor Sanjay S. Joshi, Department of Mechanical and Aeronautical Engineering, University of California, Davis, Bainer Hall, 1 Shields Avenue, Davis, California 95616, Phone: (530) 754-9662, Email: maejoshi@ucdavis.edu, Senior Member, AIAA
[‡] Distinguished Professor and Director, Spacecraft Research and Design Center, Naval Postgraduate School, Associate Fellow, AIAA
[§] Post Doctoral Research Fellow, Spacecraft Research and Design Center, Naval Postgraduate School

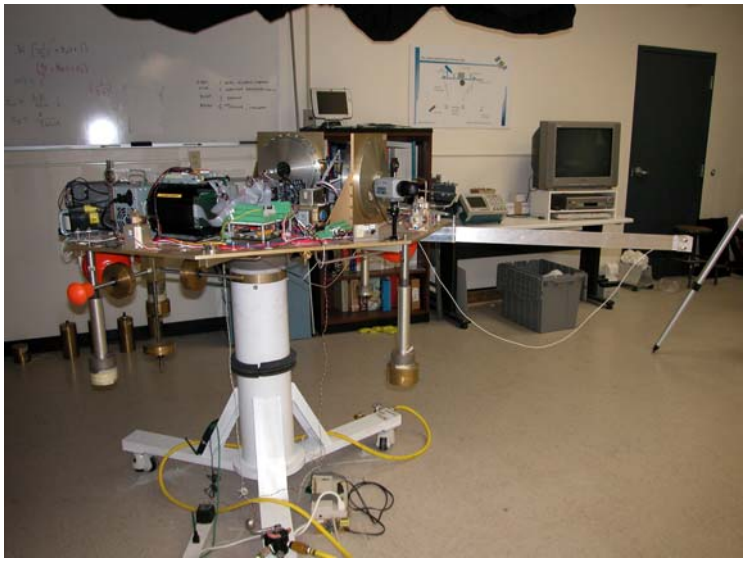

Figure 1. Naval Postgraduate School's Three-Axis Simulator (TAS).

Much research has been performed in the area of vibration suppression of flexible appendages with a variety of methods including Input Shaping, conventional Finite Impulse Response (FIR) and Infinite Impulse Response (IIR) filtering, and "dipole" Disturbance Rejection Filtering (DRF). Input Shaping, which convolves a series of impulses with the reference signal to reduce residual vibrations, has been shown to be very effective with both single degree of freedom systems (e.g. Ref. 3-4) and multiple degree of freedom systems (e.g. Ref. 5-9). In addition, its effectiveness has been experimentally validated on several systems including coordinate measuring machines, long reach manipulators, and cranes (e.g. Ref. 10-12). Conventional FIR and IIR filters have also been experimentally demonstrated to be effective in reducing residual vibrations (e.g. Ref. 13-15). Comparisons between Input Shaping and conventional filtering methods have shown Input Shaping to be more successful in some studies, and conventional filtering to be more successful in other studies, as a result of improved filter tuning[16, 17].

The current paper builds on the "dipole" disturbance rejection filter (DRF), which explicitly employs the disturbance vibration frequency into a filter embedded in the control loop. The DRF is based on the internal model principle (Ref. 18-20) and its attenuation effectiveness has been shown in a simulation of the Hubble Space Telescope[21] and in simulations for a general spacecraft with control moment gyroscopes (e.g. Ref. 22-23). The filter's effectiveness was also shown experimentally on NASA's Mini-Mast truss structure at the Langley Research Center[24] and on NASA's Advanced Control Evaluation for Structures (ACES) testbed at the Marshall Space Flight Center[25]. The Hubble Space Telescope solar array disturbance problem was also attenuated by the same filter, although the filter was not termed the "dipole" DRF[26].

The traditional DRF theory is based specifically on persistent disturbances as opposed to decaying disturbances. However, many disturbances are not persistently excited and decay before being excited again. Disturbances experienced on the TAS are such decaying disturbances, as the flexible appendage is manually deflected and released. The DRF experiments conducted on the NASA testbeds (Ref. 24-25) also appear to involve non-continuously excited (decaying) disturbances. The first experiment of the collocated design on the Mini-Mast Truss Structure involved an input impulse disturbance[24]. The ACES testbed was subjected to a step input of a hydraulically driven table, which created an overall excitation to the structure. Therefore, it appears both input disturbances actually created decaying periodic disturbances as opposed to persistent periodic disturbances because a mechanical device was not sustaining the disturbance.

This paper investigates spacecraft disturbance rejection filtering for both persistent and decaying disturbances using a realistic 3-axis spacecraft hardware testbed and associated linear and non-linear system models. The current study both validates the traditional "dipole" disturbance rejection filter and extends the results to a new class of decaying disturbances. As discussed above, although not designed specifically for decaying disturbances, prior investigations have demonstrated that the traditional "dipole" disturbance rejection filter attenuates both persistent periodic disturbances and decaying disturbances. In the following it is shown that a new filter, which we call the decaying disturbance rejection filter, also based on the internal model principle, has greater attenuation than the traditional filter for decaying disturbances. Also, it is shown that both the traditional and the new filter are not

robust to frequency uncertainty. As a result, new closed-loop system identification methods are introduced to experimentally identify the disturbance frequency to be used within the filter design for both filter types.

The paper then is organized as follows. Section II reviews the theory behind the traditional DRF. Section III develops the new filter specifically for decaying disturbances, termed the decaying disturbance rejection filter (DDRF), and compares to the traditional DRF. Section IV describes the hardware testbed and associated linear and non-linear system models. Section V demonstrates the traditional DRF and new DDRF on the testbed models. Section VI investigates robustness of the filters to frequency uncertainty. It will be shown that similar to the traditional DRF, the DDRF's attenuation effectiveness is based on accurate knowledge of the disturbance frequency (and damping ratio). Thus, Section VII introduces two methods to experimentally determine the disturbance frequency when using disturbance rejection filters, and discusses the advantages of each. Finally, Section VIII concludes the paper with a summary of results and future research directions.

II. Dipole Disturbance Rejection Filter (DRF)

A. Internal Model Principle

The "dipole" DRF is based on the internal model principle, which places disturbance poles inside the compensator loop so that the unstable disturbance poles are cancelled during loop closure between the output signal and input disturbance[18] (Fig. 2). Equation 1 shows the closed loop transfer function between the input disturbance signal, G(s), and output signal, Y(s), of Fig. 2. In closed loop, the disturbance poles are cancelled by the inclusion of a DRF.

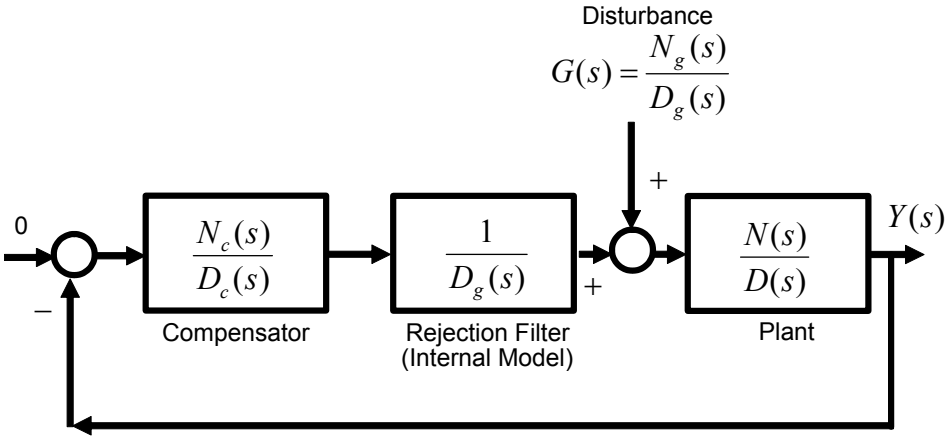

Figure 2. Closed-loop disturbance rejection control system based on internal model principle.

$$Y(s)=\frac{N(s)/D(s)}{1+N(s)N_c(s)/D(s)D_c(s)D_g(s)}G(s)=\left(\frac{D_c(s)D_g(s)N(s)}{D_c(s)D_g(s)D(s)+N_c(s)N(s)}\right)\frac{N_g(s)}{D_g(s)} \quad (1)$$

Although the traditional DRF shown in Fig. 2 does not include a numerator, a numerator with the same order as the denominator should be chosen to ensure a zero for every pole in the DRF root locus[19, 20].

To derive the traditional DRF, first consider a persistent periodic disturbance of a single frequency, which can be represented in the time domain as:

$$g_{ppd}(t)=\mathrm{A}\sin\omega t \quad (2)$$

Taking the Laplace transform of the persistent periodic disturbance results in the Laplace function:

$$G_{ppd}(s) = \frac{\omega}{s^2 + \omega^2} \tag{3}$$

where multiplying the numerator and denominator of Eq. 3 by $\left(\frac{1}{\omega^2}\right)$ results in:

$$G_{ppd}(s) = \left[\frac{\frac{1}{\omega}}{\frac{s^2}{\omega^2} + 1}\right] \tag{4}$$

Only the disturbance pole is of interest. Therefore, the persistent periodic disturbance frequency (ω) is employed as the disturbance rejection frequency (ω_p) and the DRF becomes:

$$G_{DRF}(s) = \frac{\frac{s^2}{\omega_z^2} + 1}{\frac{s^2}{\omega_p^2} + 1} \tag{5}$$

The traditional DRF numerator is included as a modification of (4), and recall that the numerator and denominator should be the same order. The traditional DRF bode plot is shown in Fig. 3 and some guidelines in selecting ω_z are provided in the next paragraph.

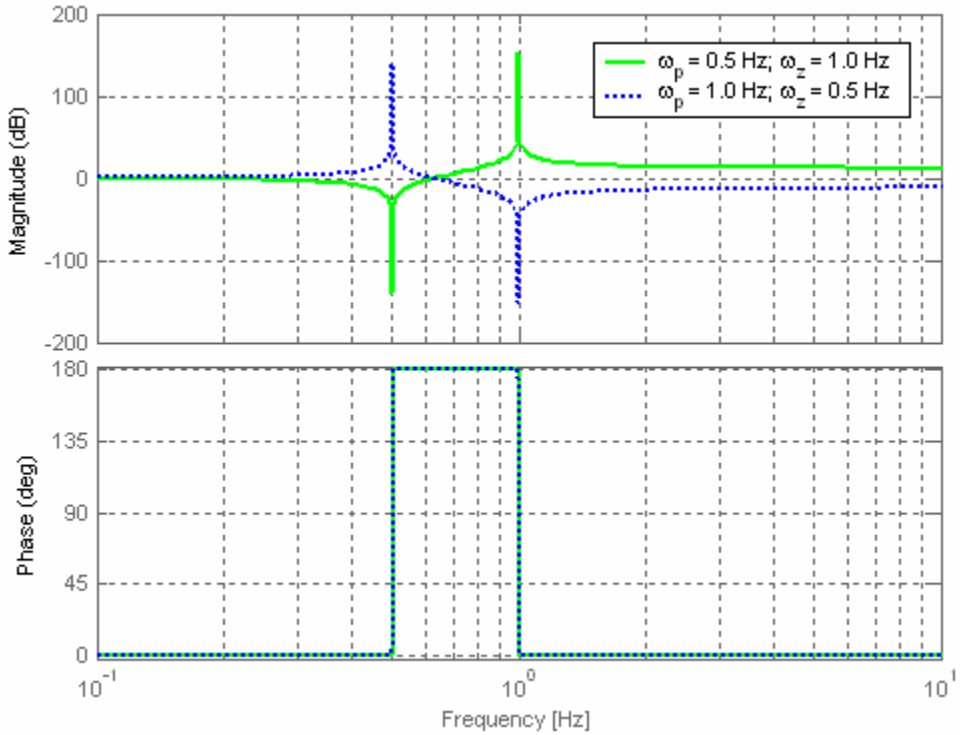

Figure 3. Traditional Disturbance Rejection Filter (DRF) Bode Diagram.

An ω_p and ω_z pair is termed a "dipole" and the difference between the ω_p and ω_z values is termed the dipole strength[20]. The settling time of the transient response increases as the difference between the dipole terms increases. The ω_z can be chosen to be less than or greater than ω_p as shown in Fig. 3. A magnitude magnification in the high frequencies results from $\omega_z > \omega_p$ and a magnitude attenuation in the high frequencies results from $\omega_z < \omega_p$. The net magnitude attenuation or magnification increases as the dipole strength increases. It is suggested that ω_z be selected to be between two consecutive poles of the system for stability [19].

$$G_c(s) = \frac{\frac{s^2}{\omega_z{}^2} + \frac{2\zeta_z}{\omega_z}s + 1}{\frac{s^2}{\omega_p{}^2} + \frac{2\zeta_p}{\omega_p}s + 1} \tag{6}$$

Shown in Eq. 5, the traditional DRF is basically a 2nd Order Generalized Filter[20], $G_c(s)$ (Eq. 6), without damping terms. Actually, damping terms can be included as reported in the literature[21]. In a Hubble Space Telescope solar array disturbance analysis, the numerator damping term was made high compared to the denominator damping term, which made the anti-resonance practically non-existent[21]. The filter was designed by adjusting the damping terms to create a 2nd Order Non-Minimum Phase Bandpass filter. Note that the damping terms in that filter were not related to the actual disturbance damping, but were used to tune the system. Finally, note that for disturbances of several frequencies, dipoles may be included for each frequency[19].

III. Decaying Disturbance Rejection Filter (DDRF)

The Decaying Disturbance Rejection Filter (DDRF) is also based on the internal model principle where the disturbance poles are placed as the DDRF poles so that the disturbance poles are cancelled during loop closure[27]. It will be shown that the DDRF has the decaying periodic disturbance's damped natural frequency as its poles. In addition to the damped natural frequency, the DDRF poles will also consider the disturbance's damping ratio (ζ) and natural frequency (ω_n). A decaying periodic disturbance signal can be represented in the time domain as:

$$g_{dpd}(t) = e^{-at}\mathrm{A}\sin\omega_d t \tag{7}$$

where A is the disturbance amplitude and $a = \zeta\omega_n$.

Taking the Laplace transform of the decaying periodic disturbance signal gives the Laplace function:

$$G_{dpd}(s) = \frac{\omega_d}{(s+a)^2 + \omega_d{}^2} \tag{8}$$

where multiplying the numerator and denominator of Eq. 8 by $\left(\frac{1}{\omega_d{}^2}\right)$ results in:

$$G_{dpd}(s) = \frac{\left(\frac{1}{\omega_d}\right)}{\frac{(s+a)^2}{\omega_d{}^2} + 1} \tag{9}$$

Based on the internal model principle, the decaying periodic disturbance pole is the only interest to the designer and the pole will be used to design a DDRF. Therefore, the decaying periodic disturbance damped natural frequency (ω_d) is employed as the disturbance rejection frequency (ω_p). Designing the DDRF numerator to have the same order as the denominator, the DDRF becomes:

$$G_{DDRF}(s) = \frac{\frac{(s+a)^2}{\omega_z{}^2} + 1}{\frac{(s+a)^2}{\omega_p{}^2} + 1} \tag{10a}$$

Multiplying out Eq. 10a and substituting $\zeta\omega_n$ for a yields Eq. 10b.

$$G_{DDRF}(s) = \frac{\frac{1}{\omega_z{}^2}s^2 + \frac{2a}{\omega_z{}^2}s + \frac{a^2+\omega_z{}^2}{\omega_z{}^2}}{\frac{1}{\omega_p{}^2}s^2 + \frac{2a}{\omega_p{}^2}s + \frac{a^2+\omega_p{}^2}{\omega_p{}^2}} = \frac{\frac{1}{\omega_z{}^2}s^2 + \frac{2\zeta\omega_n}{\omega_z{}^2}s + \frac{\zeta^2\omega_n{}^2+\omega_z{}^2}{\omega_z{}^2}}{\frac{1}{\omega_p{}^2}s^2 + \frac{2\zeta\omega_n}{\omega_p{}^2}s + \frac{\zeta^2\omega_n{}^2+\omega_p{}^2}{\omega_p{}^2}} \tag{10b}$$

Note that the decaying disturbance damping ratio (ζ) is present in the numerator and denominator of Eq. 10b. Also note that no terms are left undefined, and all are specifically related to the input disturbance. Also, note that this filter is specifically different from the traditional DRF (Eq. 5) or the "damped" DRF (Eq. 6).

IV. Naval Postgraduate School's Three-Axis Simulator (TAS) and Its Linear and Non-Linear Simulation Models

The traditional DRF, the new DDRF, and the underlying internal model principle are all based on linear system theory. Studies of both filters on linear system models have been reported (Ref. 19-20) (DRF) and (Ref. 27) (DDRF), and results validate the linear system theory as expected. In this paper, the traditional DRF and DDRF effectiveness is shown on a more realistic non-linear model to imitate the non-linearity of the experimental testbed. However, the proposed input disturbance frequency determination method discussed in Section VII will be analyzed using both a linear and non-linear simulation model.

The TAS hardware simulator's components are shown in Fig. 4. The simulator underside has a semi-spherical ball which mates with an air bearing's semi-spherical cup. The TAS essentially has three-axis frictionless motion when pressure is supplied through the air bearing, which produces a thin film of air between the semi-spherical ball and cup.

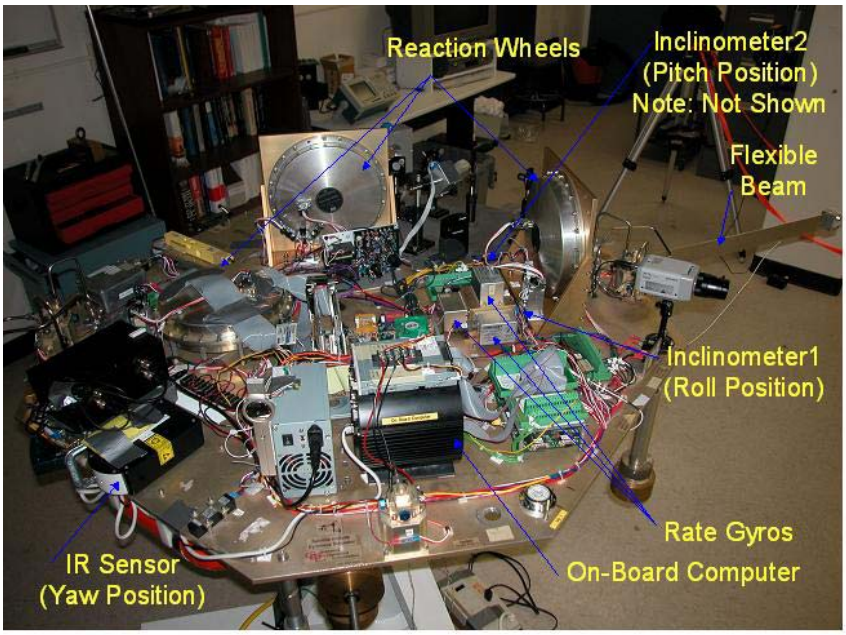

Figure 4. TAS Components.

Removable hanging masses and fine-tuning masses are utilized to balance the TAS such that the center of mass corresponds to the TAS center of rotation. In doing so, the TAS emulates a satellite in a space environment. However, perfect balancing cannot be realistically achieved by manual tuning, so a control input torque must continually counter the imbalance disturbance torque.

For actuators, the TAS has three reaction wheels, which are orthogonal to each other. The TAS uses two inclinometers and a one-axis infrared (IR) sensor for attitude sensing. The inclinometers are capacitive liquid based sensors where the sensors' capacitance is a linear function of the liquid angle. Although inclinometers are not used on actual spacecraft, inclinometers provide a reasonably accurate and inexpensive alternative to determine the TAS pitch and roll angles. The infrared sensor has two photo-transistors, which measure the change in intensity of a light source to determine the TAS yaw angle. For angular rate, the TAS uses three-orthogonal mechanical rate gyros. The TAS uses MATLAB/Simulink™ and xPC Target™ for real-time control. More details of the hardware design may be found in Ref. 27 .

The TAS is physically subjected to a decaying periodic disturbance produced from the initial displacement of an aluminum point mass and beam, which is attached to the edge of the TAS as shown in Fig. 1. The disturbance parameters are experimentally derived and are shown in Table 1[27].

™ MATLAB and xPC Target are trademarks of The Mathworks, Inc.

Parameter	Variable	Value	Units
Initial Disturbance Amplitude	A	2.1313	Nm
Disturbance Damped Natural Frequency	ω_d	0.615119287151 3.8649084672	Hz rad/s
Disturbance Natural Frequency	ω_n	0.615120919452 3.86491872324	Hz rad/s
Disturbance Damping Ratio	ζ	0.002303744	
Decay	$a = \zeta\omega_n$	0.008903784	rad/s

Table 1 Decaying Periodic Disturbance Parameters

A. TAS Single Axis Linear Simulation Model

The single axis linear TAS simulation block diagram is shown in Fig. 5. The simulation consists of a PID controller, Roll-Off Filter (ROF), disturbance rejection filter, disturbance signal, and a rigid body spacecraft plant. The transfer function for the PID controller, ROF, and plant are shown in Eqs. 11-13. The disturbance signal is either Eq. 2 or 7, depending on a persistent or decaying input disturbance. Similarly, the disturbance rejection filter is either Eq. 5 or 10b.

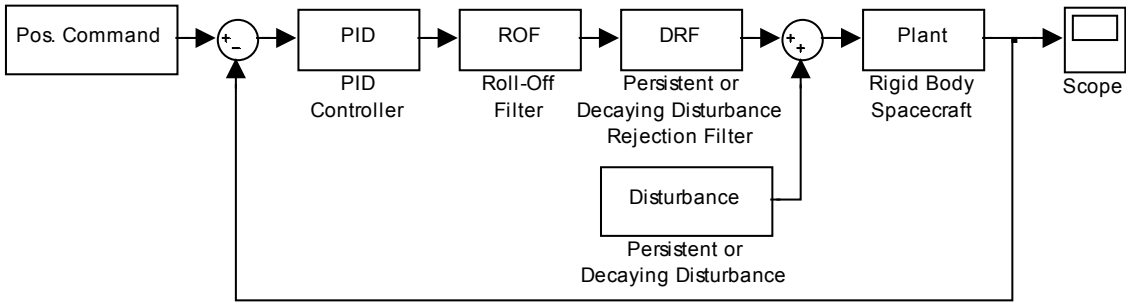

Figure 5. Closed Loop Block Diagram of Rigid Body Spacecraft with PID Controller, ROF, and DRF.

$$G_{PID}(s) = \left[\frac{\tau_d k}{s}\left(s^2 + \frac{1}{\tau_d}s + \frac{1}{\tau_d\tau_i}\right)\right] = \left[\frac{14.4686(1.1871)}{s}\left(s^2 + \frac{1}{14.4686}s + \frac{1}{14.4686(1.1871)}\right)\right] \tag{11a}$$

$$G_{PID}(s) = \left\{\frac{14.4686(1.1871)}{s}\left[s + 2\pi\left(0.005\right)\right]\left[s + 2\pi\left(0.006\right)\right]\right\} \tag{11b}$$

where k, τ_i, and τ_d are the proportional, integral and derivative PID gains, respectively.

$$G_{ROF}(s)=\left[\frac{2\pi(0.9)}{s+2\pi(0.9)}\right] \tag{12}$$

$$G_{DRF}(s)=\begin{Bmatrix}G_{PDRF}(s)\\G_{DDRF}(s)\end{Bmatrix}$$

$$G_p(s)=\left[\frac{1}{Js^2}\right]=\left[\frac{1}{55s^2}\right] \tag{13}$$

where J is the rigid body inertia about the single axis.

The PID controller and ROF were designed by shaping the frequency response plot (bode diagram) to maximize the gain and phase margins, which would ensure stability. The inertia parameter shown in Eq. 13 was experimentally determined.[27]

B. TAS 3-Axis Non-Linear Simulation Model

The 3-axis non-linear TAS simulation is based on Euler's rotational equation and the kinematic differential equation for Quaternions, which are shown in Eqs. 14 and 19, respectively[20]. Note that in our model, the roll and pitch axes (axes 1 and 3) are aligned from the central point of the testbed table through the centerlines of the pitch and roll reaction wheels shown in Fig. 4. The yaw axis (axis 2) is aligned with the vertical air bearing support structure shown in Fig. 1.

$$\boldsymbol{J}\dot{\vec{\boldsymbol{\omega}}}+\vec{\boldsymbol{\omega}}^{B/N}\times\boldsymbol{J}\vec{\boldsymbol{\omega}}^{B/N}={}^{B}\vec{\boldsymbol{T}}_{ext} \tag{14}$$

$$\begin{bmatrix}\mathrm{J}_{11}&\mathrm{J}_{12}&\mathrm{J}_{13}\\\mathrm{J}_{21}&\mathrm{J}_{22}&\mathrm{J}_{23}\\\mathrm{J}_{31}&\mathrm{J}_{32}&\mathrm{J}_{33}\end{bmatrix}\begin{bmatrix}\dot{\omega}_1\\\dot{\omega}_2\\\dot{\omega}_3\end{bmatrix}+\begin{bmatrix}0&-\omega_3&\omega_2\\\omega_3&0&-\omega_1\\-\omega_2&\omega_1&0\end{bmatrix}\begin{bmatrix}\mathrm{J}_{11}&\mathrm{J}_{12}&\mathrm{J}_{13}\\\mathrm{J}_{21}&\mathrm{J}_{22}&\mathrm{J}_{23}\\\mathrm{J}_{31}&\mathrm{J}_{32}&\mathrm{J}_{33}\end{bmatrix}\begin{bmatrix}\omega_1\\\omega_2\\\omega_3\end{bmatrix}=\begin{bmatrix}T_1\\T_2\\T_3\end{bmatrix}$$

where:

$${}^{B}\vec{\boldsymbol{T}}_{ext}={}^{B}\vec{\boldsymbol{u}}+{}^{B}\vec{\boldsymbol{T}}_{dist}+{}^{B}\vec{\boldsymbol{T}}_{imb}$$

and:

$$\boldsymbol{J}=\begin{bmatrix}31.8&5&1\\5&55&3\\1&3&31.8\end{bmatrix}\ \text{kg-m}^2 \tag{15}$$

$${}^{B}\vec{\boldsymbol{u}}=\begin{bmatrix}u_1\\u_2\\u_3\end{bmatrix}\ \text{Nm} \tag{16}$$

$${}^{B}\vec{\boldsymbol{T}}_{dist}=\begin{bmatrix}0\\e^{-0.0089t}(2.1313\sin 3.8648t)\\0\end{bmatrix}\ \text{Nm} \tag{17}$$

$$ {}^{B}\vec{T}_{imb} = \begin{bmatrix} imb_1 \\ imb_2 \\ imb_3 \end{bmatrix} \text{ Nm} \tag{18} $$

$$ \begin{bmatrix} \dot{q}_1 \\ \dot{q}_2 \\ \dot{q}_3 \\ \dot{q}_4 \end{bmatrix} = \frac{1}{2} \begin{bmatrix} 0 & \omega_3 & -\omega_2 & \omega_1 \\ -\omega_3 & 0 & \omega_1 & \omega_2 \\ \omega_2 & -\omega_1 & 0 & \omega_3 \\ -\omega_1 & \omega_2 & -\omega_3 & 0 \end{bmatrix} \begin{bmatrix} q_1 \\ q_2 \\ q_3 \\ q_4 \end{bmatrix} \tag{19} $$

where $\vec{q} = \begin{bmatrix} q_1 & q_2 & q_3 & q_4 \end{bmatrix}^T$, $\dot{\vec{q}} = \begin{bmatrix} \dot{q}_1 & \dot{q}_2 & \dot{q}_3 & \dot{q}_4 \end{bmatrix}^T$ and $\vec{\omega} = \begin{bmatrix} \omega_1 & \omega_2 & \omega_3 \end{bmatrix}^T$.

Figure 6 shows the 3-Axis Non-Linear TAS Simulink model used to analyze the traditional DRF and new DDRF. An attitude command is given, which is then transformed to a rate command from the relation for a 2-3-1 rotation sequence shown in Eq. 20 [20].

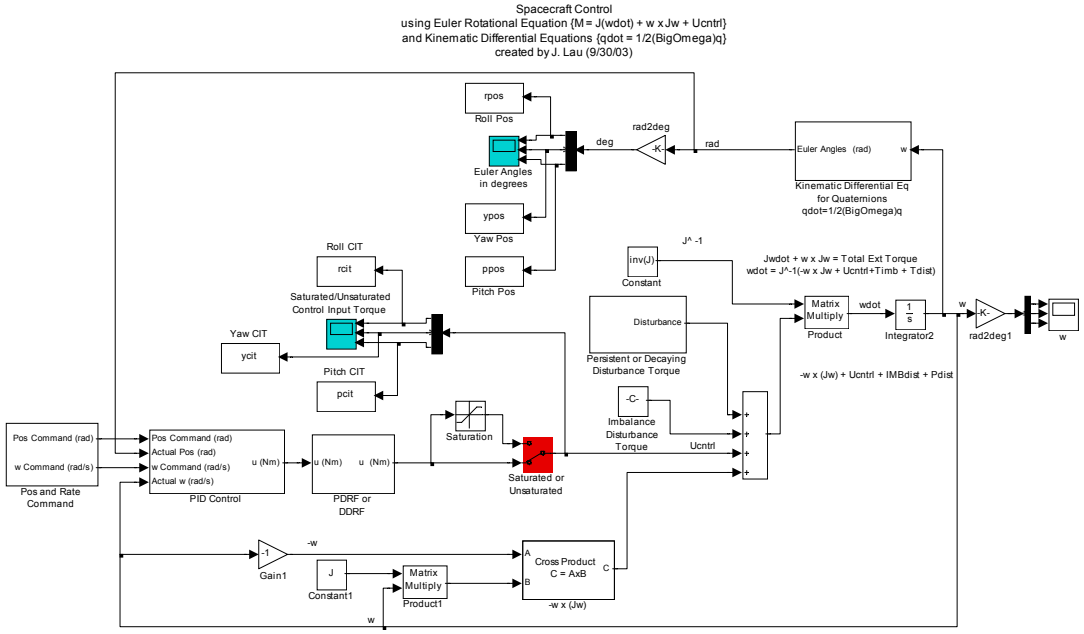

Figure 6. 3-Axis Non-Linear TAS Simulation Model.

$$ \begin{bmatrix} \dot{\theta}_1 \\ \dot{\theta}_2 \\ \dot{\theta}_3 \end{bmatrix} = \frac{1}{\cos\theta_3} \begin{bmatrix} \cos\theta_3 & -\cos\theta_1 \sin\theta_3 & \sin\theta_1 \sin\theta_3 \\ 0 & \cos\theta_1 & -\sin\theta_1 \\ 0 & \sin\theta_1 \cos\theta_3 & \cos\theta_1 \cos\theta_3 \end{bmatrix} \begin{bmatrix} \omega_1 \\ \omega_2 \\ \omega_3 \end{bmatrix} \tag{20} $$

The measured or actual rate is solved by Euler's rotational equation, which is shown in Eq. 14. The rate is then fed back so a rate error signal is calculated by taking the difference between the commanded and actual rate. At the same time, the actual rate is used in Eq. 19 to calculate the actual attitude in quaternions. The quaternion vector is transformed to Euler angles where the actual attitude is fed back to the commanded attitude so the attitude error signal is calculated. The conversion from quaternions to Euler angles for a 2-3-1 rotational sequence is shown

in Eqs. 21 - 23. The attitude and rate error signals are utilized in PID control. A control input torque (CIT) is generated after a DRF (Eq. 24) or DDRF (Eq. 25) depending on whether the filter design is considering a persistent or decaying input disturbance (Fig. 2).

$$\theta_2 = \tan^{-1}\left[-\frac{2\left(q_1 q_3 - q_2 q_4\right)}{1-2\left(q_2{}^2 + q_3{}^2\right)}\right] \tag{21}$$

$$\theta_3 = \sin^{-1}\left[2\left(q_1 q_2 + q_3 q_4\right)\right] \tag{22}$$

$$\theta_1 = \tan^{-1}\left[-\frac{2\left(q_3 q_2 - q_1 q_4\right)}{1-2\left(q_1{}^2 + q_3{}^2\right)}\right] \tag{23}$$

The total external torque shown in Eq. 14 includes the control input torque, TAS imbalance disturbance torque, and a persistent or decaying periodic disturbance torque about the yaw axis. All of the torques are in the spacecraft body frame and are represented in the Simulink model shown in Fig. 6.

The TAS imbalance disturbance torques shown in Eq. 18 were approximated using the hardware testbed's CIT experimental data and are each on the order of 0.1 Nm. The imbalance torque is the result of the center of mass not coinciding with the center of rotation. This effect changes slightly depending on the success of each balancing of the testbed. A bias in the CIT experimental data approximates the magnitude of imbalance being countered (Fig. 14). For spacecraft, the imbalance disturbance torque parameters can be more precisely obtained via coasting maneuvers[28]. For the inertia matrix shown in Eq. 15, the inertia about the yaw axis was experimentally determined[27]. The inertia about the pitch and roll axes were analytically determined and are also described in Ref. 27. The products of inertia were assumed small compared to the diagonal inertias. Small values were estimated so coupling between the axes would also be small, based on the assumption that our coordinate system is close to the principal axes. To numerically verify the final 3-Axis Simulation (3-AS), the sum of all torques in the zero command case was verified as zero as expected from theory[27].

V. Effect of DRF and DDRF in TAS Non Linear Model

Knowing the decaying periodic input disturbance's damped natural frequency, natural frequency, and damping ratio from Table 1, the DDRF is expressed as shown in Eq. 25. When considering a persistent periodic input disturbance in the simulation, the decaying disturbance's damped natural frequency will be used as the persistent disturbance frequency. Therefore, the traditional DRF is expressed as shown in Eq. 24. The ω_z selected for both filters follows the guideline of being between two consecutive poles[19]. The ω_z is placed between one of the plant poles at the origin and the DRF's or DDRF's pole.

$$G_{DRF}(s) = \frac{\frac{s^2}{\omega_z{}^2}+1}{\frac{s^2}{\omega_p{}^2}+1} = \frac{\frac{s^2}{\left[2\pi\left(0.5\right)\right]^2}+1}{\frac{s^2}{\left[2\pi\left(0.6151\right)\right]^2}+1} = \frac{0.1013\mathrm{s}^2+1}{0.06695\mathrm{s}^2+1} \tag{24}$$

$$G_{DDRF}(s)=\frac{\frac{(s+a)^2}{\omega_z{}^2}+1}{\frac{(s+a)^2}{\omega_p{}^2}+1}=\frac{\frac{[s+0.0089]^2}{[2\pi(0.5)]^2}+1}{\frac{[s+0.0089]^2}{[2\pi(0.6151)]^2}+1}=\frac{0.1013s^2+0.001804s+1.0000252}{0.06695s^2+0.001192s+1.00000531} \quad (25)$$

Equations 24 and 25 are employed in Fig. 6 depending if the filter is designed considering a persistent or decaying disturbance. Evaluating Eqs. 24 and 25, it can be seen that the DDRF form looks like the traditional DRF form with damping terms. However, it should be noted again that the DDRF damping terms are specifically dependent on ζ, ω_n, and ω_p, and are not arbitrary tuning or shaping parameters as in the 2nd order generalized filter[20].

Figure 7 shows the traditional DRF's effectiveness on a persistent periodic input disturbance in the yaw. The attitude command is a one-degree position command in the yaw and a 0-degree position command in the pitch and roll to emulate the TAS stabilization process. This result again validates the results of several previous studies of the DRF (e.g. Ref. 21-23).

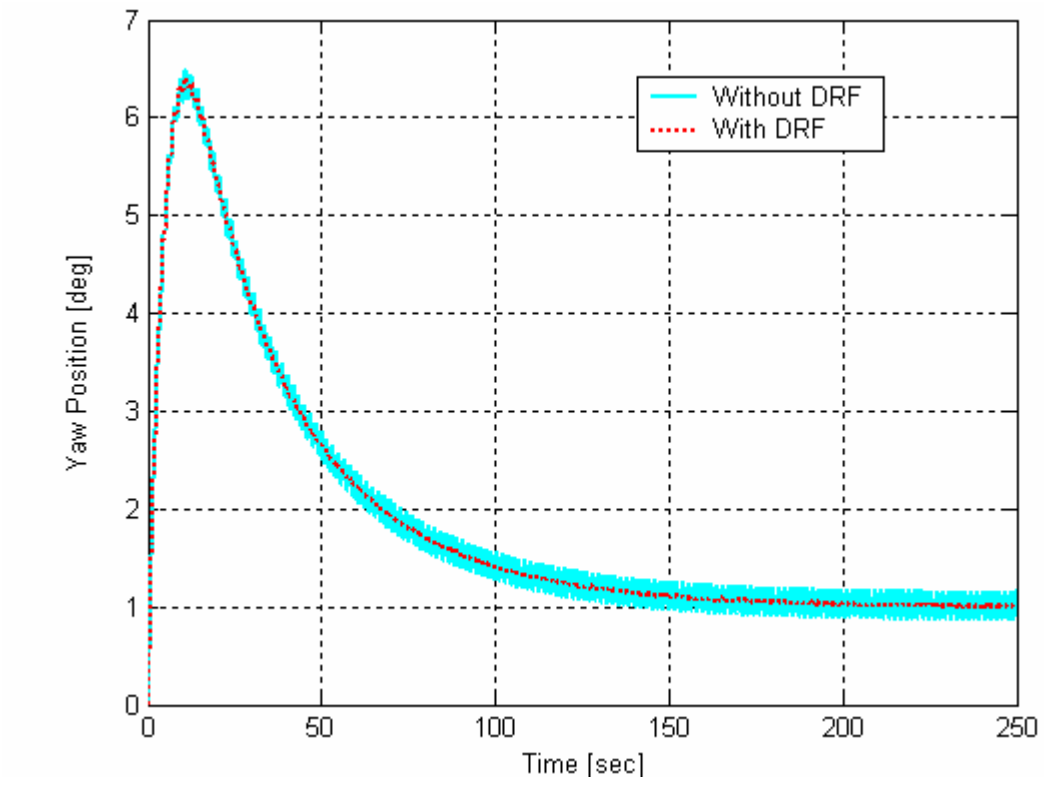

Figure 7. Traditional DRF Effect on Persistent PD of 0.6151 Hz and 2.13 Nm Peak Magnitude in 3-AS.

We now consider the response of both the traditional DRF and new DDRF to the *decaying* periodic disturbance defined in Table 1. Although not explicitly presented, the traditional DRF has been experimentally demonstrated in past research to attenuate decaying periodic disturbances[24, 25]. Figure 8 shows that the traditional DRF does attenuate some of the decaying periodic disturbance as shown in past studies, but the new DDRF's attenuation is superior. Figure 9 combines Fig. 8 and zooms in on the last 20 seconds to show the DRF and DDRF's effectiveness on a decaying periodic input disturbance in the yaw. The control input torque is of comparable magnitude using either filter, with the DDRF using slightly less torque.

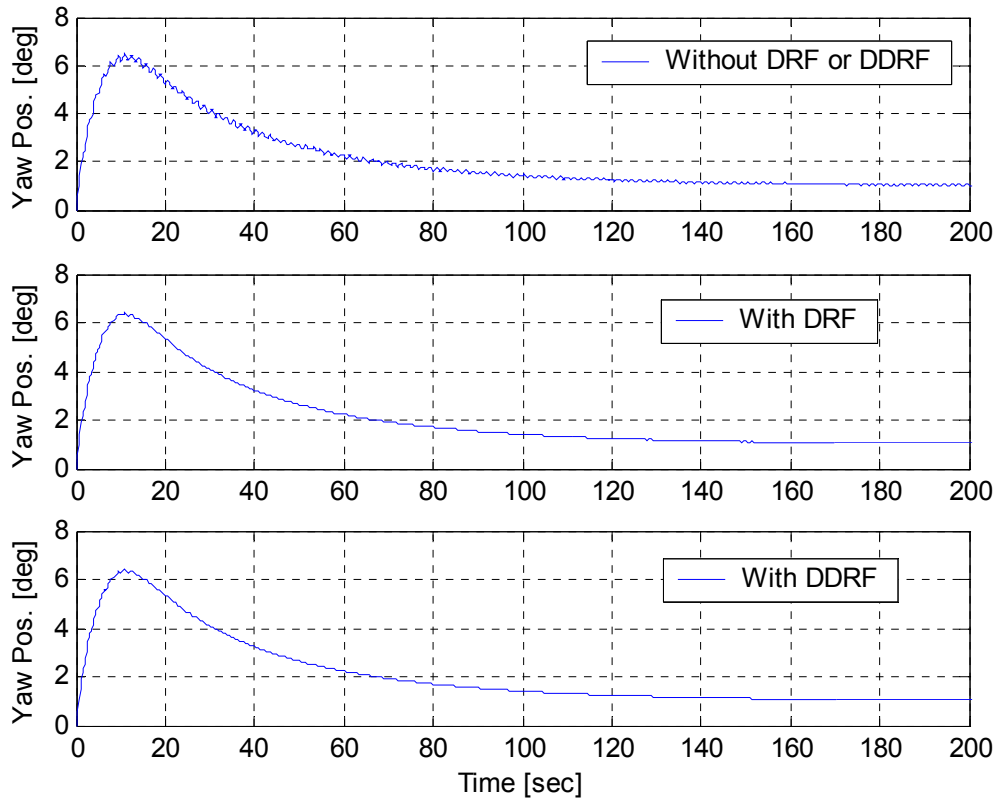

Figure 8. Traditional DRF and DDRF Effect on *Decaying* PD of 0.6151 Hz and 2.13 Nm Initial Peak Magnitude in 3-AS.

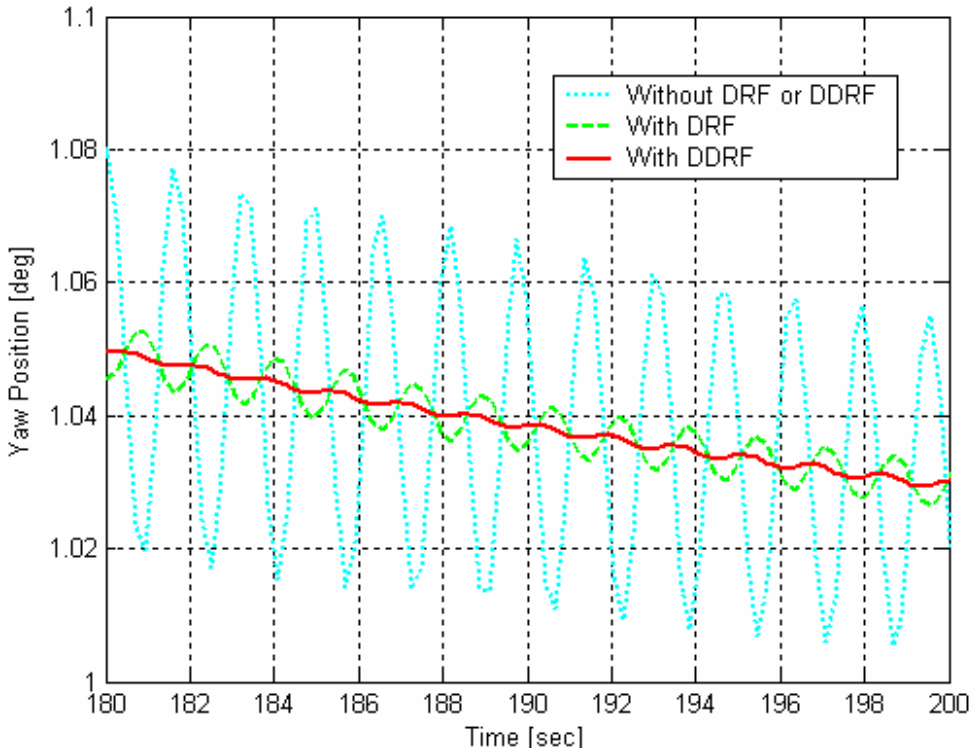

Figure 9. Traditional DRF and DDRF Effect on *Decaying* PD of 0.6151 Hz and 2.13 Nm Initial Peak Magnitude in 3-AS (Zoom-In)

It should be noted that we were not able to show the new decaying disturbance rejection filter working on the hardware testbed directly as a result of actuator saturation. Our reaction wheel actuators were limited to 0.2 Nm, while our required torque was 2.13 Nm.

VI. DRF and DDRF Robustness to Frequency Uncertainty

Figures 7 – 9 showed the traditional DRF and DDRF's capability in attenuating persistent and decaying periodic input disturbances. However, the results are based on the assumption that the designer exactly knows the disturbance frequency. The disturbance frequency is not usually exactly known. Figures 10 and 11 show the output position response when the traditional DRF and DDRF frequency does not exactly match the input disturbance frequency.

Figure 10 compares the response when the traditional DRF rejects the correct and incorrect decaying input disturbance frequencies. The traditional DRF is not very robust as there is no attenuation when the traditional DRF rejection frequency is incorrect by +/- 0.1 Hz (approximately 15% frequency uncertainty). Figure 11 compares the response when the DDRF also rejects the correct and incorrect decaying input disturbance frequencies. The disturbance is almost completely eliminated when the DDRF rejects the correct disturbance frequency of 0.6151 Hz. If the DDRF rejection frequency is incorrect by 0.1 Hz, the results are similar to Fig. 10. Therefore, neither the traditional DRF nor the DDRF are very robust to frequency uncertainty. In the next section, we will introduce new system identification methods to explicitly determine the filter design frequency.

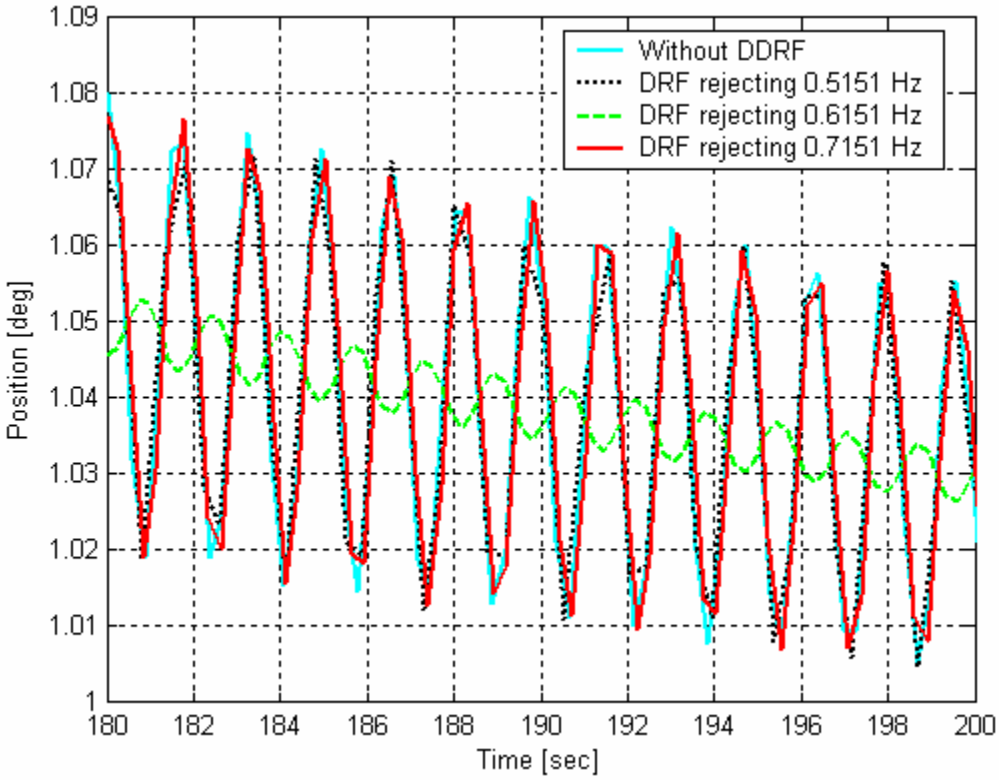

Figure 10. Traditional DRF Rejection Frequency Varies where Decaying PD is 0.6151 Hz in 3-AS

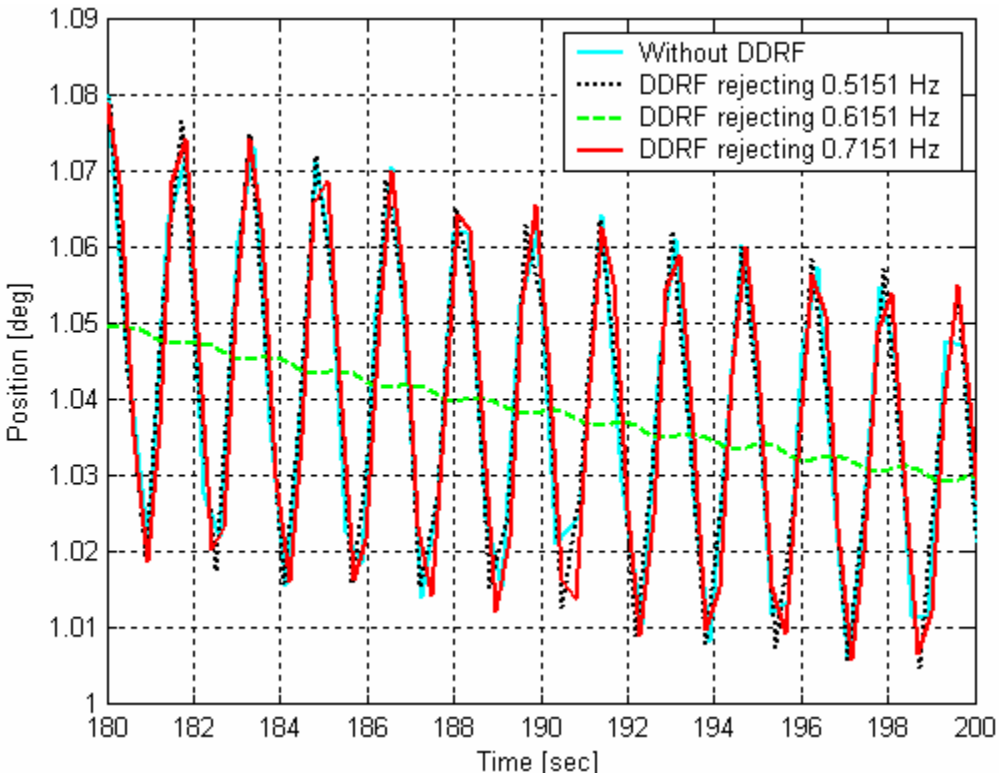

Figure 11. DDRF Rejection Frequency Varies where Decaying PD is 0.6151 Hz in 3-AS.

Knowledge of damping terms is also important for the DDRF (Eq. 10b), as inaccurate damping terms will reduce the effectiveness of the DDRF. However, note that when damping is incorrectly estimated as zero, the DDRF (Eq. 10b) reverts to the DRF (Eq. 5) and the filter is still somewhat effective as seen in Fig. 8. Increased damping reduces the control input torque (CIT), which also reduces disturbance rejection[27].

VII. Input Disturbance Frequency Determination

It was shown in the 3-axis simulation that the traditional DRF and the DDRF are not very robust to frequency uncertainty. If the input disturbance frequency is not exactly known, the traditional DRF and DDRF's attenuation is negligible. Therefore, the ability to determine the input disturbance frequency is essential for the designer. In this section, two closed-loop methods to determine the input disturbance frequency will be shown. The first method evaluates the control input torque (CIT) plot and simply counts the number of cycles in a time range. The second method exploits a beating phenomena in the CIT that results from an inaccurate filter design frequency. Both methods will be demonstrated in linear and non-linear simulations, as well as hardware experiments.

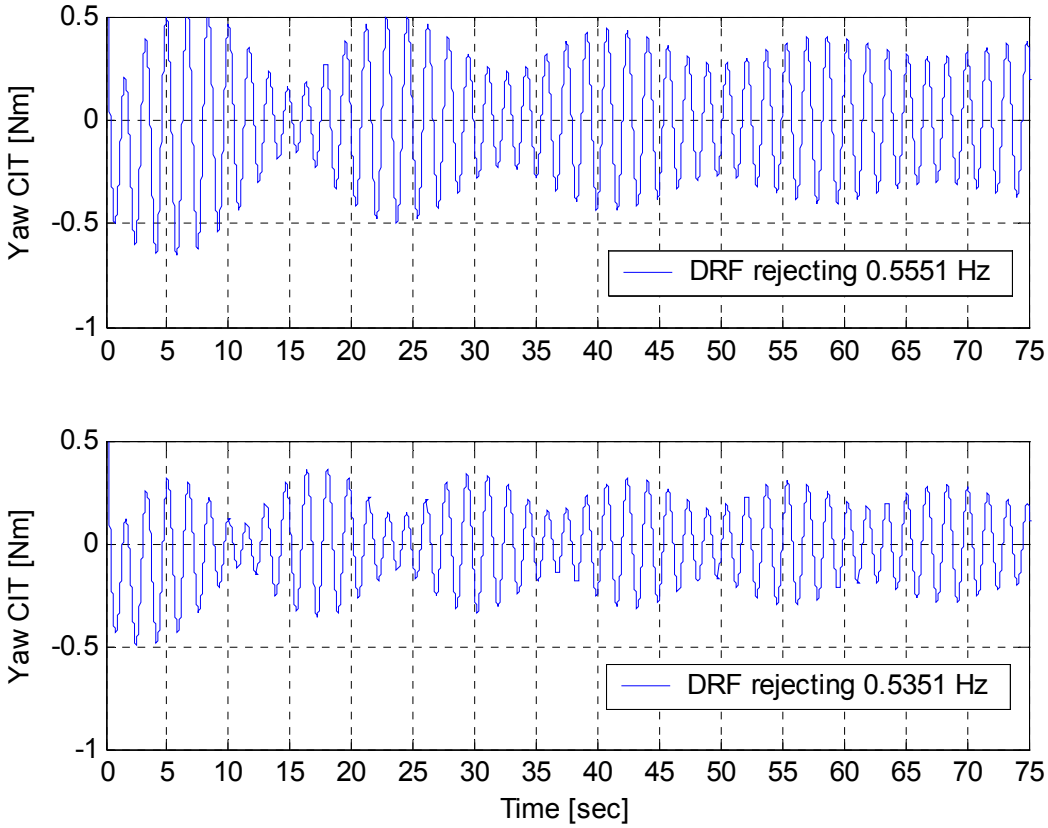

Figure 12. Yaw CIT when Traditional DRF Rejection Frequency is not Equivalent to Disturbance Frequency in 1-AS (Persistent Disturbance Frequency = 0.6151 Hz).

Figure 12 shows the CIT plot from the single-axis linear simulation (Fig. 5). The top portion of Figure 12 shows the CIT in closed-loop from the linear model when the traditional DRF is designed using a 0.5551 Hz disturbance rejection frequency (ω_p) and the bottom portion shows the CIT in closed-loop when the traditional DRF is designed using a 0.5351 Hz disturbance rejection frequency (ω_p), where the actual input disturbance frequency for both is 0.6151 Hz. For the top and bottom plots of Fig. 12, ω_z is 0.5 Hz.

For the first frequency determination method, the input disturbance frequency can be found by measuring the high frequency oscillation in Fig 12. This high-frequency oscillation in the top and bottom plots both reveal the input disturbance frequency of 0.6151 Hz.

Shown in Fig. 12, it is also interesting to note that the "beating" phenomenon is occurring, which is the superposition of two waves with slightly differing frequencies[29]. Through linear and non-linear simulation studies and hardware testbed experiments, it has been found that if the filter *design* frequencies obey the relation to the actual disturbance frequencies as

$$\omega_z < \omega_p < \text{ Actual Disturbance Frequency}$$

in Eq. 5, then beats appear in the CIT plot. For Fig. 12, recall that ω_p is 0.5551 Hz and 0.5351 Hz for the top and bottom plots, respectively. The bottom portion of Fig. 12 shows more beats than the top portion and also shows a decrease in CIT. Therefore, as ω_p approaches ω_z, which is 0.5 Hz, more beats occur in the CIT and the CIT decreases. If ω_p reached ω_z then Eq. 5 would equate to 1 as if the rejection filter were not used. As ω_p approaches the actual input disturbance frequency, less beats occur and the CIT increases to approach the disturbance amplitude[27].

To validate the "beating" phenomenon of the linear system, disturbances and filters were investigated in both the 3-axis non-linear simulation model and on the actual hardware testbed. The CIT plot from the non-linear simulation using the same disturbance and filter conditions of Fig. 12 is shown in Fig. 13. Note that beating is once again present. The input disturbance of Fig. 13 is a persistent disturbance. Beats also occur if the input disturbance is decaying, and when using the DDRF on the decaying disturbance[27].

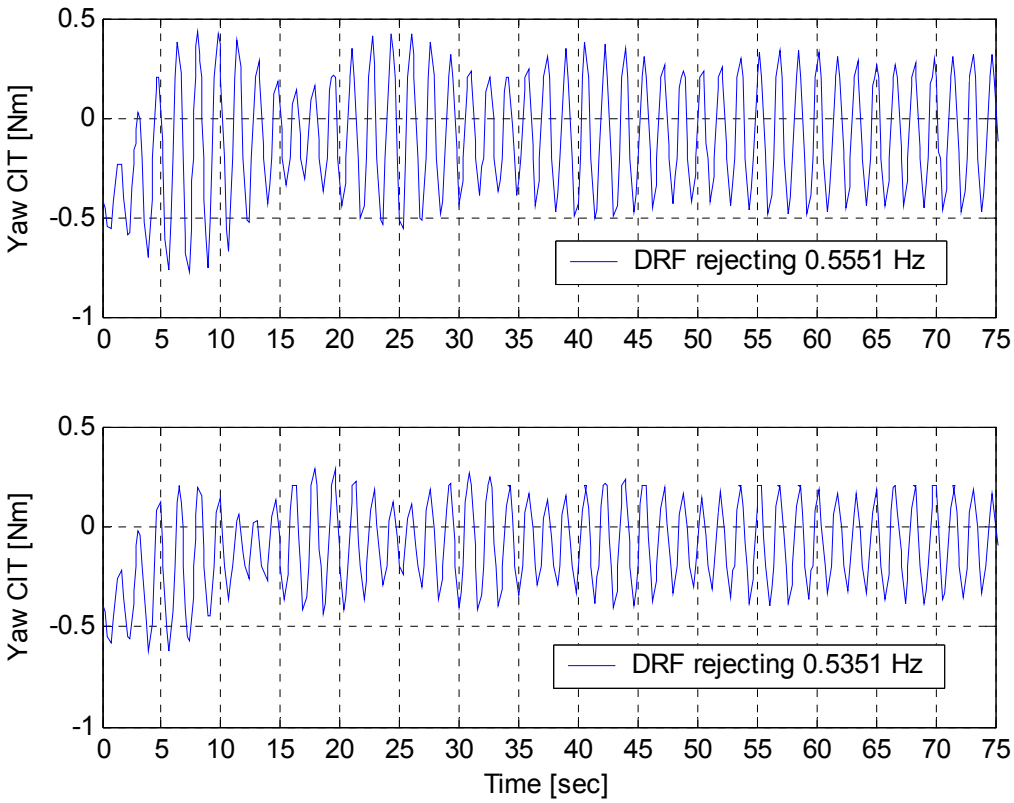

Figure 13. Yaw CIT when Traditional DRF Rejection Frequency is not Equivalent to Disturbance Frequency in 3-AS (Persistent Disturbance Frequency = 0.6151 Hz).

The same phenomenon was also experimentally validated on the hardware TAS. The hardware TAS parameters are equivalent to the simulation parameters (which are originally derived from the TAS testbed). Below, the TAS attempts to maintain an Euler angle attitude of $\begin{bmatrix} 0 & 0 & 0 \end{bmatrix}^T$ while experiencing a decaying periodic input disturbance. The disturbance frequency is 0.6151 Hz and the traditional DRF rejection frequency is 0.5551 Hz. The resulting CIT response is shown in Fig. 14. Again, beats are present.

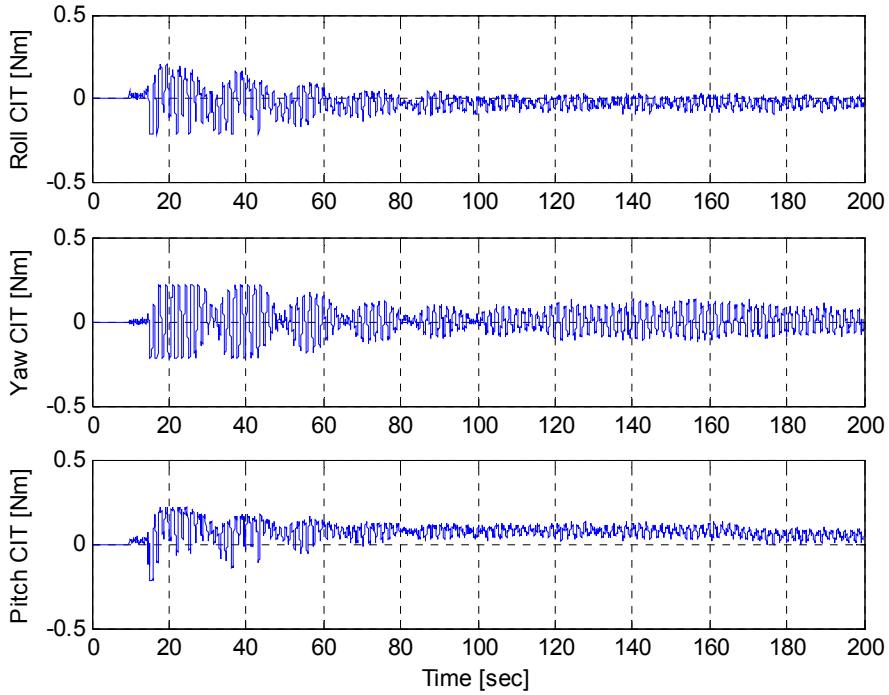

Figure 14. Experimental CIT Responses for 0.6151 Hz Decaying PD when Traditional DRF rejection frequency is 0.5551 Hz. Note that the pitch CIT is biased due to an imbalance of the testbed.

A frequency determination method employing a traditional DRF and CIT beats will now be shown using the non-linear simulation results (Fig. 13). Note that the method could have been demonstrated with either the linear simulation (Fig. 12) or the hardware experiment results (Fig. 14). The CIT beat frequency (f_b), actual input disturbance frequency (f_{dist}), and DRF rejection design frequency (f_{DRF}) are known to be related by:

$$f_b = f_{dist} - f_{DRF} \tag{26}$$

It should be noted that Eq. 26 is simply describing the definition of a beat frequency. Therefore, in this case, the beat frequency is produced by the slightly differing frequencies of the actual input disturbance frequency and the filter rejection frequency. In the top portion of Fig. 13, the beat frequency is shown to be:

$$f_{b1} = \frac{1.5}{50-25} \left[\frac{\text{beats}}{\text{sec}}\right] = 0.06 \text{ Hz}$$

and in the bottom portion of Fig. 14, the beat frequency is:

$$f_{b2} = \frac{2}{37.5-12.5} \left[\frac{\text{beats}}{\text{sec}}\right] = 0.08 \text{ Hz}$$

where f_{DRF1} is 0.5551 Hz for the top portion and f_{DRF2} is 0.5351 for the bottom portion of Fig. 13. Substituting f_{DRF1} and f_{b1} into Eq. 26:

$$f_{b1} = f_{dist} - f_{DRF1}$$
$$f_{dist} = f_{b1} + f_{DRF1}$$
$$f_{dist} = 0.06 + 0.5551$$
$$f_{dist} = 0.6151 \text{ Hz}$$

And substituting f_{DRF2} and f_{b2} into Eq. 26:

$$f_{b2} = f_{dist} - f_{DRF2}$$
$$f_{dist} = f_{b2} + f_{DRF2}$$
$$f_{dist} = 0.08 + 0.5351$$
$$f_{dist} = 0.6151 \text{ Hz}$$

Note that the first method, evaluating the high frequency oscillation to determine the input frequency, could have been performed on any of the CIT plots. One would again find the input disturbance frequency to be 0.6151 Hz.

Therefore, if the filter designer has an estimate of the actual input disturbance frequency, the designer can use a "close" DRF rejection frequency to produce beats in the CIT and explicitly determine the actual disturbance frequency. Notice that the simple system identification method can be implemented whether the plant is on-site or remote such as on an orbiting satellite.

Comparing the two frequency determination methods, there are some advantages to utilizing the method employing beats. Using the proposed beats method, the designer is able to easily visualize if the rejection frequency (ω_p) is correct or not. If beats appear, then ω_p is incorrect. As the designer alters ω_p, either more or less beats will appear. As previously stated, if ω_p is increased towards the actual disturbance frequency, less beats will occur and the CIT magnitude will increase to the input disturbance magnitude.[27] Therefore, by employing the beats to determine the input disturbance frequency, the designer has two simple visual trends that reveal if the rejection frequency is correct; (1) decrease in beats and (2) increase in CIT magnitude. Although not developed further here, these trends could also be automated to tune the filters on-orbit, which would be especially helpful if the disturbance frequency was changing over time. These methods are applicable to both persistent and decaying disturbances. However, for the case of decaying disturbances, the quality of the disturbance frequency identification will clearly be dependent on the amount of time the disturbance manifests itself.

VIII. Conclusion

This paper investigated spacecraft disturbance rejection for both persistent and decaying disturbances using the Naval Postgraduate School 3-Axis spacecraft simulator. It built on the "dipole" disturbance rejection filter, based on the internal model principle. Although not designed specifically for decaying disturbances, prior investigations have demonstrated that the traditional "dipole" disturbance rejection filter attenuates both persistent periodic disturbances and decaying disturbances. In this paper, we developed a new filter, closely related to the traditional filter, which we call the decaying disturbance rejection filter. The new filter, also based on the internal model principle, was shown to have greater attenuation than the traditional filter for decaying disturbances on the Naval Postgraduate School 3-axis simulator non-linear model. Also, it was shown that both the traditional and the new filter are not robust to frequency uncertainty. Designing either filter with an error of 15% in the disturbance frequency essentially renders the disturbance filters ineffective. As a result, two closed-loop system identification methods were introduced to experimentally identify the disturbance frequency to be used within the filter design for both filter types. One system identification procedure takes advantage of the phenomenon that when a faulty frequency is used to design either filter, beating appears in the input control torque. The beat frequency is related to the actual disturbance frequency. Two natural extensions of this work would make for valuable further work. First, as noted earlier, we could not validate our DRF methods directly on the hardware testbed due to actuator saturation in our reaction wheels. In fact, the needed reaction wheel torque is related to the disturbance magnitude, which

saturated our current reaction wheels. A study of the affect of actuator saturation on DRF methods would be useful. Also, we noted earlier that our closed-loop methods of frequency identification could be used to create automatic DRF filter tuning on-board orbiting spacecraft. This could be especially helpful if the disturbance frequency was changing over time. One promising method could be to indirectly ascertain beating by examining the CIT frequency response via a FFT. The formalization of an integrated DRF, system ID, and system tuning architecture would be valuable.

Acknowledgement

We would like to gratefully acknowledge Professor Bong Wie of Arizona State University for helpful email correspondence. We would also like to thank the anonymous reviewers for their valuable comments and suggestions.

References

[1]Agrawal, B.N., "Acquisition, Tracking, and Pointing of Bifocal Relay Mirror Spacecraft," American Astronautical, Feb. 2003, AAS 03-151.

[2]Agrawal, B.N., Romano, M., and Martinez, T., "Three Axis Attitude Control Simulators for Bifocal Relay Mirror Spacecraft," Advances in the Astronautical Sciences, 2003, AAS 03-268.

[3]Singer, N., and Seering, W., "Preshaping Command Inputs to Reduce System Vibration," Journal of Dynamic Systems, Measurement and Control, Vol. 112, No. 1, 1990, pp. 76-82.

[4]Singhose, W., Porter, L.J., Tuttle, T.D., And Singer, N.C., "Vibration Reduction Using Multi-Hump Input Shapers," Journal of Dynamic Systems, Measurement and Control, Vol. 119, No. 2, 1997, pp. 320-326.

[5]Singh, T., and Heppler, G.R., "Shaped Input Control of a System with Multiple Modes," Journal of Dynamic Systems, Measurement and Control, Vol. 115, No. 3, 1993, pp. 341-347.

[6]Singh, T., and Vadali, S.R., "Robust Time-Delay Control of Multi-Mode Systems," International Journal of Control, Vol. 62, No. 6, 1995, pp. 1319-1339

[7]Lim, S., Stevens, H.D., and How, J.P., "Input Shaping Design for Multi-Input Flexible Systems," Journal of Dynamic Systems, Measurement and Control, Vol. 121, No. 3, 1999, pp. 443-447.

[8]Pao, L.Y., "Input Shaping Design for Flexible Systems with Multiple Actuators," Proceedings of the 1996 IFAC World Congress, Pergamon, Oxford, U.K., pp. 267-272

[9]Tuttle, T.D., and Seering, W.P., "A Zero Placement Technique for Designing Shaped Inputs to Suppress Multiple–Mode Vibrations," Proceedings of the 1994 American Control Conference, IEEE Press, New York, pp. 2533-2537.

[10]Jones, S.D., and Ulsoy, A.G., "Approach to Control Input Shaping with Application to Coordinate Measuring Machines," Journal of Dynamic Systems, Measurement and Control, Vol. 121, No. 2, 1999, pp. 242-247

[11]Magee, D.P., and Book, W., "Filtering Micro-Manipulator Wrist Commands to Prevent Flexible Base Motion," Proceedings of the 1995 American Control Conference, American Automatic Control Council, Evanston, IL, pp. 924-928

[12]Singer, N., Singhose, W., and Kriikku, E., "An Input Shaping Controller Enabling Cranes to Move Without Sway," Proceedings of the 1997 ANS Topical Meeting on Robotics and Remote Systems, American Nuclear Society, La Grange Park, IL, 1997, pp. 225-231

[13]Economou, D., Mavroidis, C., and Antoniadis, I., "Experimental Demonstration of Input Preconditioning for Residual Vibration Suppression Using Low-Pass FIR Digital Filters," Proceedings of the American Control Conference, Arlington, VA June 25-27, 2001, pp. 1581-1586

[14]Economou, D., Mavroidis, C., and Antoniadis, I., "Experiments of Robust Vibration Suppression in Mechatronic Systems Using IIR Digital Filters," 2001 IEEE/ASME International Conference on Advance Intelligent Mechatronics Proceedings, Como, Italy, July 8-12, 2001, pp. 731-737.

[15]Economou, D., Mavroidis, C., and Antoniadis, I., "Maximally Robust Input Preconditioning for Residual Vibration Suppression Using Low-Pass FIR Digital Filters," Journal of Dynamic Systems, Measurement and Control, Vol. 124, No. 1, 2002, pp. 85-97

[16]Singer, N., Singhose, W., and Seering, W., "Comparison of Filtering Methods for Reducing Residual Vibration," European Journal of Control, 5, 1999, pp. 208-218.

[17]Economou, D., Mavroidis, C., and Antoniadis, I., "Comparison of Filter Types Used for Command Preconditioning in Vibration Suppression Applications," Proceedings of the American Control Conference, Anchorage, AK, May 8-10, 2002, pp. 2273-2278.

[18]Chen, C., Linear System Theory and Design, Oxford University Press, New York, 1999, Chap. 8.3.1, pp. 243-247.

[19]Wie, B., and Gonzalez, M., "Control Synthesis for Flexible Space Structures Excited by Persistent Disturbances," Journal of Guidance, Control, and Dynamics, Vol. 15, No. 1, Jan-Feb 1992, pp. 73-80.

[20]Wie, B., Space Vehicle Dynamics and Control, AIAA Educational Series, AIAA, Reston, Virginia, 1998.

[21]Wie, B., Liu, Q., and Bauer, F., "Classical and Robust H□ Control Redesign for the Hubble Space Telescope," Journal of Guidance, Control, and Dynamics, Vol. 16, No. 6, Nov-Dec 1993, pp. 1069-1077

[22]Heiiberg, C.J., Bailey, D., and Wie, B., "Precision Control Moment Gyroscope Spacecraft Control with Disturbance," Society of Photo-Optical Instrumentation Engineers, Paper 3041-93, San Diego, March 1997.

[23]Heiberg, C.J., Bailey, D., and Wie, B., "Precision Spacecraft Pointing Using Single-Gimbal Control Moment Gyroscopes with Disturbance," Journal of Guidance, Control, and Dynamics, Vol. 23, No. 1, Jan-Feb 2000, pp. 77-85.

[24]Wie, B., Horta, L., and Sulla, J., "Classical Control System Design and Experiment for the Mini-Mast Truss Structure," Journal of Guidance, Control, and Dynamics, Vol. 14, No. 4, 1991, pp. 778-784.

[25]Wie, B., "Experimental Demonstration of a Classical Approach to Flexible Structure Control," Journal of Guidance, Control, and Dynamics, Vol. 15, No. 6, Nov-Dec 1992, pp. 1327-1333.

[26]Nurre, G.S., Sharkey, J.P., Nelson, J.D., Bradley, A.J., "Preservicing Mission, On-Orbit Modifications to Hubble Space Telescope Pointing Control System," Journal of Guidance, Control, and Dynamics, Vol. 18, No. 2, Mar-Apr 1995, pp. 222-229.

[27]Lau, J., "Spacecraft Attitude Control and Disturbance Rejection", UC Davis MS Thesis, Department of Mechanical and Aeronautical Engineering, December 2004.

[28]Tanygin, S., Williams, T., "Mass Property Estimation Using Coasting Maneuvers," Journal of Guidance, Control, and Dynamics, Vol. 20, No. 4, Jul-Aug 1997, pp. 625-632.

[29]Serway, R.A., Physics For Scientists & Engineers, Harcout Brace & Company, Orlando, Florida, 1992, pp. 492-495.